Available online at www.sciencedirect.com
SCIENCE DIRECT®
ELSEVIER
Icarus 167 (2004) 453–463
ICARUS
www.elsevier.com/locate/icarus

Scattering from a fractal surface: acoustical experiments and comparison with near-nadir models

Stéphanie Gautier and Dominique Gibert *

Géosciences Rennes (CNRS UMR 6118), University Rennes 1, 35042 Rennes cedex, France

Received 15 April 2003; revised 1 October 2003

Abstract

A homogeneous resin print of the surface of a naturally-fractured granite block with an experimental Hurst exponent $H \simeq 0.7$ is placed in a water tank. An acoustical source insonifies the surface in a near-nadir direction and the backscattered waves are recorded near the source. Such measurements are made at different positions along a profile above the surface in order to obtain the energy spectrum of the mean backscattered wavefield. The wavelength range considered is $0.58 \leqslant \lambda \leqslant 8.72$ mm in water. A synthetic energy spectrum is obtained from a model [Shepard and Campbell, Icarus 141 (1999) 156] which represents the rough surface as an ensemble of point scatterers and assumes a single-scattering regime. This model reasonably fits with the experimental spectrum with the largest discrepancies observed for $\lambda < 2.5$ mm. The fit is improved in the whole wavelength interval by accounting for the long-range topography variations occurring along the averaging profile.

Keywords: Geophysics; Fractal surfaces; Experimental techniques; Backscattering

1. Introduction

The understanding of the origin and evolution of rough planetary surfaces largely relies on the use of remote sensing methods and, in particular, on the analysis of scattered radar waves. The characterization of rough surfaces from backscattered waves involves an inverse approach where the roughness properties of the surface are recovered by comparing forward-model outputs with the information brought by the recorded wavefield. It is then of importance to dispose of reliable modeling methods to compute the synthetic waves backscattered by a given rough surface. The particular parameterization retained for the forward modeling depends both on the nature of the experimental data to be inverted (e.g., time domain versus spectral domain) and on the geometrical and statistical description used to represent the rough surfaces. Concerning the latter point, numerous studies have established the fractal nature of many natural rough surfaces (e.g., Sayles and Thomas, 1978; Mandelbrot, 1982; Bouchaud et al., 1990; Hastings and Sugihara, 1993) whose main characteristics are long-range correlations and nonstationary statistical behavior. The nonstationarity occurs at all observation scales and is responsible of particular phenomena concerning the backscattering of waves. For instance, fractal variations of topography make the mean backscattered wavefield to vanish as the length of the averaging profile goes to infinity. More generally, an important difficulty encountered with waves backscattered by fractal surfaces is that mean physical quantities vanish as the size of the averaging domain increases. As a consequence, whatever the size of an experiment (i.e., averaging area, number of averaged measurement points, frequency band, ...) the classical asymptotic approximations (e.g., short or long wavelengths, effective media, ...) will never be reached for all observation scales. Consequently, as observed in many experimental instances, the physical phenomena of interest belong to mesoscopic physics where individual experiments display strong fluctuations from one to another. Such a situation is not considered in the numerous studies where rough surfaces are represented as moderate random deviations from a reference plane (see, e.g., Voronovich, 1994, for a recent review). Up to now, a comparatively small number of studies have considered wave scattering by self-affine rough surfaces where the long-range topography variations produce large destructive interference phenomena at all wavelengths (e.g., Shepard et al., 1995; Shepard and Campbell, 1999; Simonsen et al., 2000).

* Corresponding author.
E-mail address: gibert@univ-rennes1.fr (D. Gibert).

0019-1035/$ – see front matter © 2003 Published by Elsevier Inc.
doi:10.1016/j.icarus.2003.10.004

In the present study, we detail and discuss underwater acoustical backscattering experiments with a self-affine rough surface whose topography is measured with a profile laser scanner. Acoustical waves are used instead of vector electromagnetic waves in order to produce data which directly compare with already published scalar-wave models. The energy spectrum of the averaged backscattered wavefield is measured in the 172 kHz $\leqslant f \leqslant$ 2.572 MHz frequency range, i.e., for wavelengths $0.58 \leqslant \lambda \leqslant 8.72$ mm in water. This spectrum is compared to a Kirchhoff backscattering model recently proposed by Shepard and Campbell (1999) where the surface is represented as an ensemble of point scatterers and assuming single scattering. It is shown that this model fits with the data excepted in the short-wavelength domain. The fit is improved by accounting for the long-range topography variations occurring at the mesoscopic scales along the averaging profile.

2. Description of the experimental rough surface

2.1. Statistical quantities characterizing rough surfaces

Natural rough surfaces are often considered as realizations of random processes and the quantification of their roughness characteristics extensively relies on the use of statistical methods (Sayles and Thomas, 1978). Both the Euclidean concept and the fractal geometry paradigm provide the basis of useful statistical models of rough surfaces (Mandelbrot, 1982; Brown, 1987; Power and Tullis, 1987, 1991, 1992; Korvin, 1992; Cox and Wang, 1993; Turcotte, 1997). Euclidean models consider rough surfaces as random variations of the height with respect to an Euclidean reference surface commonly chosen to be a plane. For such models the roughness is described by the statistical properties of the random height variations which are assumed stationary, and the statistical properties do not vary with respect to both the observation scale L and the position R on the surface. While many man-made rough surfaces are reasonably well described by Euclidean models, most natural rough surfaces instead do not satisfy the stationarity hypothesis and their statistical attributes depend on the observation scale L at which the statistics are done. Such surfaces often verify a statistical homogeneity property which may be written as (Mandelbrot, 1982; Feder, 1988)

$$L \to \lambda L \quad \Longrightarrow \quad \Delta h \to \lambda^H \Delta h, \tag{1}$$

where Δh is the height range statistically observed at the observation scale L. For instance, Δh may be the average range spanned by the vertical axis when plotting a region of width L. The homogeneity parameter H is the Hurst exponent and, for profiles, is such that $0 \leqslant H \leqslant 1$. Rough surfaces satisfying Eq. (1) are said to be self-affine (self-similar if $H = 1$) and are described by fractal models which account for the scale dependence of their statistical quantities.

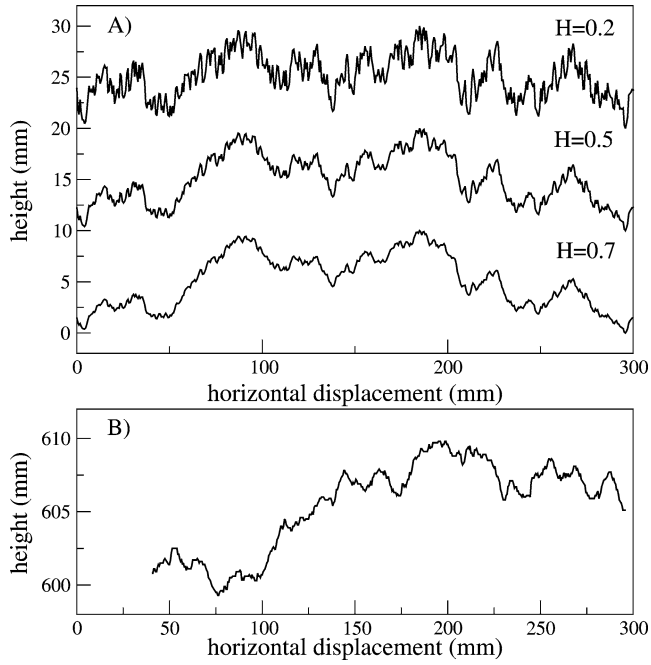

Fig. 1. (A) Three synthetic self-affine profiles with different Hurst exponents showing the roughness dependence with respect to H. All three profiles have been generated by the Fourier transform method and have the same random phase spectrum. This explains the common appearance of the profiles. (B) Example of a profile (in the y direction) extracted from the experimental rough surface used in the present study.

The Hurst exponent H may be replaced by the commonly used fractal dimension which is given by,

$$D = d - H, \tag{2}$$

where d is the dimension of the embedding Euclidean space ($d = 2$ for a profile and $d = 3$ for a surface) (Shepard et al., 1995; Shepard and Campbell, 1999).

The roughness appearance of a self-affine surface strongly depends on the value of its Hurst exponent which controls the relative importance of the range of height variations among the observation scales. For instance, Fig. 1A shows several synthetic self-affine profiles generated with the Fourier synthesis method (Mehrabi et al., 1997) where the energy spectrum of the profile is a power law with an exponent $2H + 1$ and the phases are uniformly distributed in $(-\pi, +\pi)$. In order to better appreciate the effect of H on the roughness appearance, the same random phase spectrum is used for all profiles. It can be observed that the Hurst exponent affects the rate at which the roughness changes with scale: the smaller H the larger the relative variations of the small-scale topography.

Among the different statistical quantities which may be computed to characterize the fractal nature of a rough surface, the root mean square height $\xi(L)$ (RMS height) is commonly used to quantify the height distribution (Shepard et al., 1995),

$$\xi(L) = \sqrt{\langle (h - \bar{h})^2 \rangle}, \tag{3}$$

where $\langle\cdot\rangle$ denotes the average over an ensemble of profiles, $\bar{h}$ is the mean height of each individual profile, and L is the observation scale at which the statistical attributes are computed. In the literature dealing with rough surfaces, the scale L is generally understood as being the length of a straight profile along which the rough topography is measured (e.g., Feder, 1988). However, in the present study, the observation scale is not restricted to this simple concept and, when necessary, it will also be taken as the length of circular profiles. For self-affine topography variations, the statistical homogeneity property (1) may be used to rewrite the RMS height defined by Eq. (3) as

$$\xi(L) = \xi(L_0)\left(\frac{L}{L_0}\right)^H, \tag{4}$$

where L_0 is an arbitrary reference scale.

Another useful statistical parameter is the RMS deviation, ν, also called the structure function or the variogram or the Allan deviation, and defined as the RMS height difference between two points separated by a distance ΔR:

$$\nu(\Delta R) = \sqrt{\left\langle \big(z(R) - z(R+\Delta R)\big)^2 \right\rangle}, \tag{5}$$

where $\langle\cdot\rangle$ denotes the average over an ensemble of positions R. The RMS deviation is frequently converted to the RMS slope,

$$s_{\mathrm{rms}}(\Delta R) = \frac{\nu(\Delta R)}{\Delta R}. \tag{6}$$

For self-affine surfaces satisfying the homogeneity property (1), both ν and s_{rms} have the following scale dependences (Campbell and Shepard, 1996; Shepard and Campbell, 1999; Shepard et al., 2001):

$$\nu(\Delta R) = \nu(\Delta R_0)\left(\frac{\Delta R}{\Delta R_0}\right)^H \tag{7}$$

and

$$s_{\mathrm{rms}}(\Delta R) = s_{\mathrm{rms}}(\Delta R_0)\left(\frac{\Delta R}{\Delta R_0}\right)^{H-1}, \tag{8}$$

where ΔR_0 is an arbitrary reference distance.

In the remainder of this paper the studied rough surfaces are assumed fractal-like with statistical attributes supposed to obey the power laws given by Eqs. (4), (7) and (8). As noted above, the observation scale L along which the variations of topography are considered will not be restricted to its most common definition, i.e., the length of a straight segment, but it will also be defined as the perimeter L_c of a circle along which the surface topography is sampled. A circular sampling of the rough surface naturally occurs in the models discussed in the present paper in order to account for the fact that the beam forming the incident acoustical wave produces a quasi-circular spot onto the rough surface to be probed. Hence, a good choice is the cylindrical coordinates system where the beam spot is represented as a sum of concentric annuli with radii $0 \leqslant r \leqslant r_{\mathrm{A}}$ and with circumferences $L_c = 2\pi r$ which are the relevant observation scales. The radius, r_{A}, of the Airy–Fresnel spot is the critical radius such that the waves reradiated by the concentric annuli $r > r_{\mathrm{A}}$ do not significantly contribute to the constructive interferences giving the measured backscattered wavefield. This critical radius depends on both the wavelength of the incident wave and the roughness, i.e., the Hurst exponent H, of the surface. The knowledge of the radius r_{A} of the Airy–Fresnel spot is of importance since it represents the elementary area, i.e., the resolution pixel, of the rough surface probed by the incident wave.

2.2. Experimental rough surface

The experimental rough surface used in the present study has been produced from a naturally fractured block of granite extracted from the Lanhélin quarries located in Brittany (France). In order to eliminate the volume scattering effects due to the mineral grains forming the granite sample, the scattering experiments are performed with a homogeneous resin print of a 315×334 mm^2 region of the natural surface (Fig. 2). The thickness of the resin sample is sufficiently large (i.e., 100 mm) to allow a clear separation of the waves reflected by the rough top surface from those reflected by the flat bottom face of the sample.

A numerical topography map of the rough surface was done with a profile laser scanner, resulting in a 512×512 regular grid with a square regular sampling of 0.5 mm and a precision of about 0.3 mm in the vertical direction (Darboux and Huang, 2003). A profile extracted from the numerical grid is shown in Fig. 1B and a comparison with the synthetic self-affine profiles (Fig. 1A) indicates that the Hurst exponent of the natural surface is near 0.70. The RMS heights $\xi_X(L)$ and $\xi_Y(L)$ computed from the numerical grid are shown in Fig. 3 for straight sampling along profiles in the

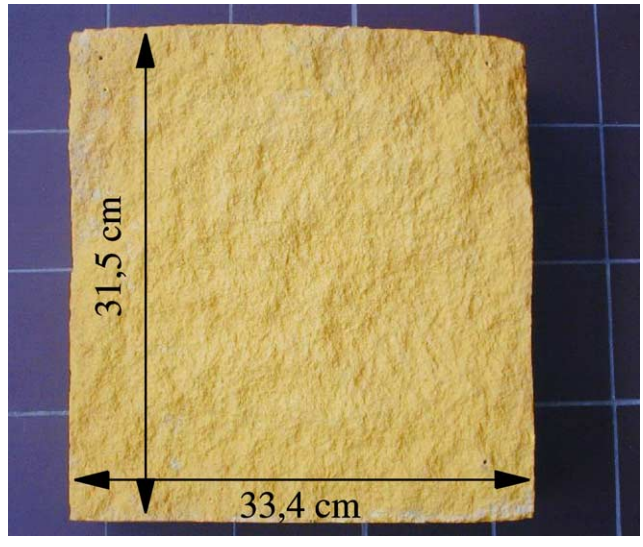

Fig. 2. Top view of the resin print of the rough granite sample. The thickness of the sample is greater than 100 mm in order to separate the waves reflected by the top rough surface from those coming from the flat bottom face.

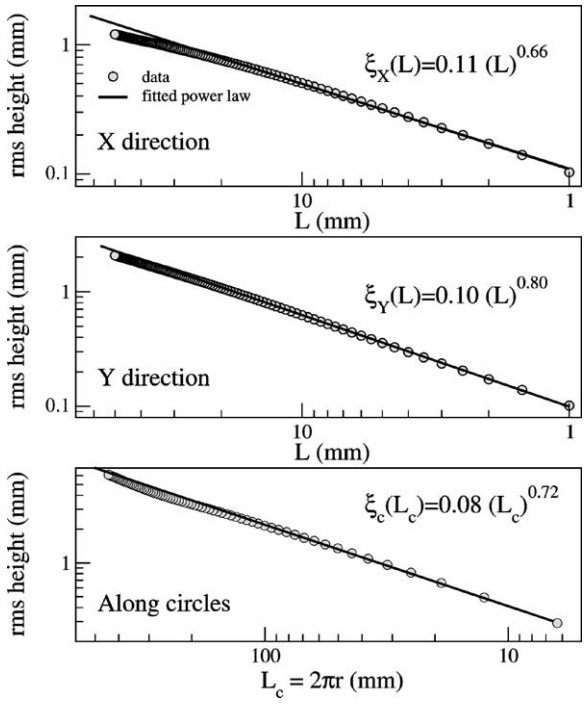

Fig. 3. RMS height $\xi(L)$ (see Eq. (3)) shown as a function of the profile length L along which the topography is sampled. The solid lines correspond to theoretical power laws fitted with the short-scale part of the data and extrapolated to the whole scale range. At small scales, the three curves display a power-law appearance whose slope (in a log–log plot) gives the Hurst exponent H (Eq. (4)). At larger scales, the experimental curves slightly depart from the pure power laws. The top and middle curves are for the RMS height computed for profiles oriented in the x and y directions, respectively. The Hurst exponent H differs for both directions, indicating a slight roughness anisotropy. The RMS height curve shown at the bottom of the figure is computed from the topography sampled along circles of radius $r = L_c/2\pi$ and has a Hurst exponent value intermediate between the ones found for the x and y directions.

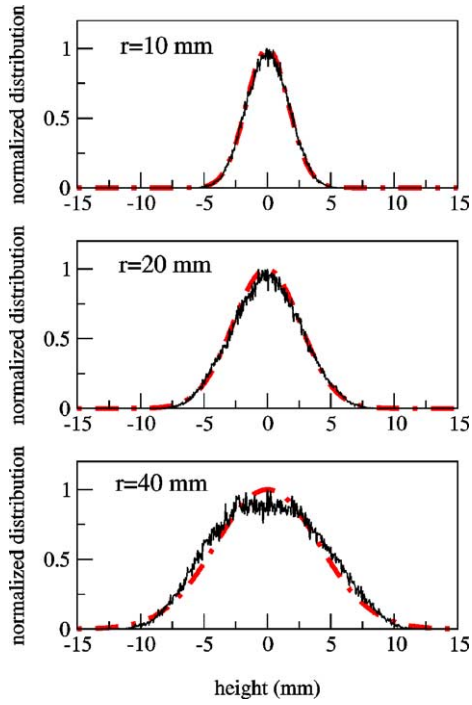

Fig. 4. Histograms of height values of the rough surface sampled along circles of radius $r = 10$, 20, and 40 mm together with their best-fitting Gaussian curves (dashed lines). The height is measured with respect to the center of the circles.

x and y directions. A circular sampling of the surface is also done by computing the RMS height $\xi_c(L_c)$ from the topography sampled along circles with circumference being taken as the observation length $L_c = 2\pi r$. All three curves display a typical power-law appearance confirming the self-affine geometry of the natural surface. It can be observed that the Hurst exponent differs for the x ($H_X \simeq 0.66$) and y ($H_Y \simeq 0.80$) directions indicating a slight roughness anisotropy with a rougher topography in the x direction. The Hurst exponent obtained for the isotropic circular sampling has an intermediate value ($H_c \simeq 0.72$) in accordance with the estimates obtained by other authors for similar natural surfaces (Brown and Scholz, 1985; Bouchaud et al., 1990; Poon et al., 1992; Schmittbuhl et al., 1995; Bouchaud, 1997). Figure 4 shows the histograms of the height values sampled on circles with radii $r = 10$, 20, and 40 mm. A comparison with the best-fitting Gaussian curves shows that the height distributions may reasonably be assumed random Gaussian with a standard deviation given by the $\xi_c(r)$ power law shown at the bottom of Fig. 3.

3. Near-nadir scattering experiments

A summary sketch of the experimental setup is shown in Fig. 5: an arbitrary waveform generator triggers a power amplifier which fires a piezoelectric source (also called a projector in the acoustical literature) directed toward the rough surface in the nadir direction. The waves reflected by the surface are recorded with another piezoelectric transducer (called a hydrophone) located near the source. The signals received by the hydrophone are directed toward an A/D converter and digitized with a 12 bits resolution and at a 50 MHz sampling rate. All numerical data are stored in the computer in order to allow further processing. Figure 6 shows the frame used to perform the measurements. In the present experiments, both the projector and the hydrophone are placed in the far field and vertically above the surface (approximately 600 mm). The surface can be horizontally translated in order to perform a straight scan along y profiles of length $L = 185$ mm. Let us emphasize that since the projector and the hydrophone are fixed onto the rigid frame, their distance l_e with respect to the surface is not a constant and varies along the profile. The whole system is placed in a large water-tank (5 m^3) in order to get rid of the waves reflected by the tank sides.

The goal of the experiment is to record the energy spectrum of the waves reflected by the rough surface. In practice, this cannot be done by using sinusoidal wavetrains of long duration because the so-recorded spectrum would not only concern the rough surface itself but also the bottom face

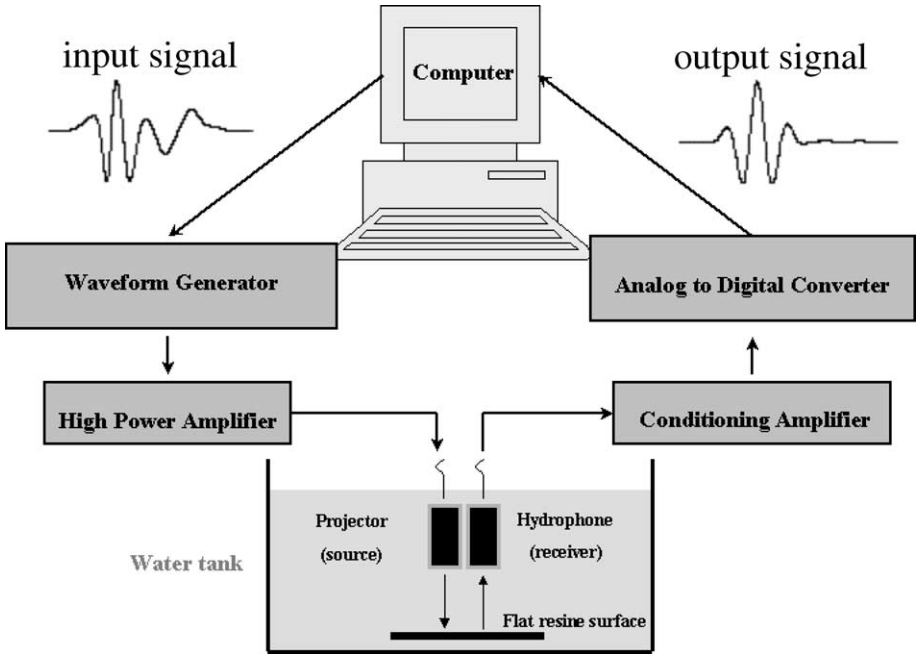

Fig. 5. Schematic view of the setup used for the near-nadir experiments made up of a source line (arbitrary waveform generator, power amplifier and projector) and a receiving line (hydrophone, preamplifier and A/D converter), both connected to the computer. The input signals are sent to the power amplifier through an arbitrary waveform generator driven by the computer. The output signals are recorded through an A/D converter connected to the computer. A flat and smooth resin print is used during the preliminary calibrating experiment where the source signals are inverted in order to produce output signals corresponding to a wavelet family. An example of actual input/output signals is given. When the calibrating experiment is completed the smooth resin sample is replaced by the rough resin surface and the family of input signals is sent to the projector to obtain the wavelet response of the rough surface.

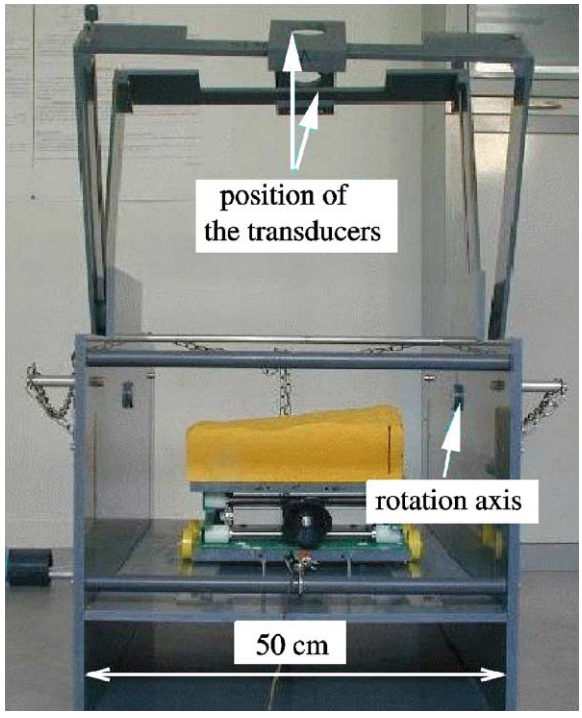

Fig. 6. Lateral view, in the (x, z) plane, of the experimental frame to be placed in the water tank. The rough surface may be translated along the y direction perpendicular to the picture. In the present experiment, the two arms holding the piezoelectric transducers are vertically oriented to be in a near-nadir geometry with a bi-static angle of 5° between the projector and the hydrophone.

of the sample and parts of the rigid frame. In order to restrict the measurements to the rough surface of interest, it is necessary to isolate this subsystem from the remaining parts of the whole apparatus. This may be done in the physical space-time by using source signals sufficiently localized on the time axis so that the waves reflected by the rough surface may easily be isolated from echoes coming from the other parts of the experimental system. The counterpart of this solution is that the source signals cease to be pure sinusoidal ones with a well-defined single frequency but instead are, at best, a truncated sinusoid with a band-pass spectrum of finite (and hopefully narrow) bandwidth. In the present experiments, we use source signals defined as wavelets $\Psi_a(t)$ with a constant shape,

$$\Psi_a(t) = \frac{1}{a}\frac{\mathrm{d}^4}{\mathrm{d}(t/a)^4}\exp\left(-\frac{t^2}{a^2}\right), \tag{9}$$

where the dilation $a > 0$ controls the central frequency $f_c \propto a^{-1}$ of the wavelet.

In order to obtain accurate signals with a high signal-to-noise ratio, a preliminary calibrating experiment is done by recording the waves reflected by a flat horizontal reference surface. During the calibrating experiment, a nonlinear and iterative optimization procedure is used to find which input signals (Fig. 5) must be emitted by the projector to produce output signals corresponding to the desired wavelets $\Psi_a(t)$. A great advantage of this experimental procedure is that all linear and/or nonlinear distortions produced by the apparatus are automatically corrected and that no deconvo-

lution of the output signals is necessary during the remaining experiments. By this way, very clean and controlled signals are obtained with a high signal-to-noise ratio which enables a precise analysis of the frequency-dependent response of the target (Le Gonidec et al., 2002; Conil et al., 2003). For the present calibrating experiment, input signals have been inverted for seven pairs of transducers in order to have a wavelet family covering the frequency band 172 kHz $\leqslant f \leqslant$ 2.572 MHz, i.e., corresponding to wavelengths $0.58 \leqslant \lambda \leqslant 8.72$ mm in water. The central frequency of the wavelets varies from $f_c = 250$ kHz to $f_c = 2.5$ MHz.

After the completion of the calibrating experiment, the flat reference surface is replaced by the rough surface and the calibrated input signals are sent to the power amplifier in exactly the same conditions (i.e., settings of electronic elements, distances, etc.) as during the calibrating experiment. The waves reflected by the rough surface are recorded at a discrete number of positions along an horizontal y profile. The collection of signals recorded at a single location on the y profile constitutes what will hereafter be called an individual wavelet response of the target surface. A total of 75 such individual wavelet responses have been recorded along a 185-mm long y profile at a constant sampling interval $\Delta y = 2.5$ mm. In the present study, the individual wavelet responses have been averaged to obtain the mean wavelet response used to compute the energy spectrum of the mean backscattered waves. The averaging is performed in the time domain by summing the raw signals available at each frequency. The Fig. 7 shows the energy spectra obtained by averaging a variable number n of consecutive individual wavelet responses. It can be observed that the larger n the steeper the energy decrease at short wavelengths. This n-dependence of the energy falloff is an indicator of the self-affine geometry of the rough surface and results from the fact that the longer the averaging segment

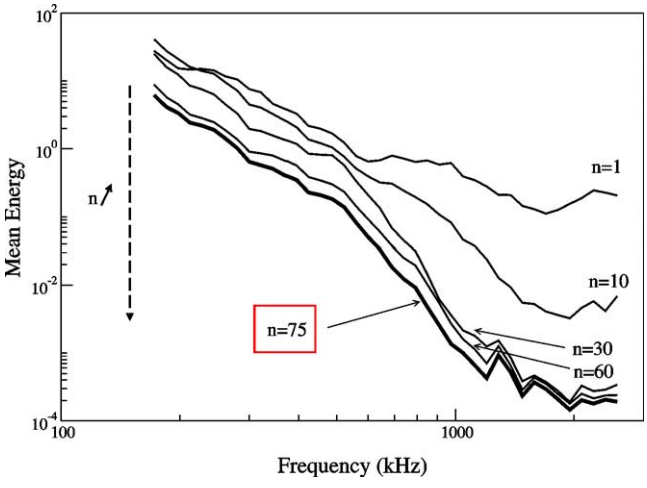

Fig. 7. Plots of the mean backscattered energy computed for an increasing number n of individual wavelet responses. The mean-energy spectra quickly converge toward a common profile as the number n of averaged wavelet responses increases. The $n = 75$ profile is the one analyzed in the present study.

the stronger the energy annihilation by destructive interferences. For $n \geqslant 60$, i.e., an averaging length $L \geqslant 147.5$ mm, the slope of the curves does not significantly change, and the $n = 75$ curve is the one studied in the remaining of this paper.

4. Huygens modeling of the mean backscattered field

In this section we present the main characteristics of the mean backscattered field model to be compared with the data obtained during the scattering experiments. This model was initially proposed by Shepard and Campbell (1999) and assumes a monochromatic plane-wave of wavelength λ at normal incidence and with amplitude Ψ_0. The time dependence $\exp(-i\omega t)$ will be omitted hereafter. The backscattered wavefield reflected by the rough self-affine surface is received at a point P located in the far field above the surface (Fig. 8). The rough surface is represented as an ensemble of point scatterers S excited by the incident plane wave. Single scattering is assumed and the Helmholtz–Kirchhoff diffraction formula (Goodman, 1968; Elmore and Heald, 1985; Ogilvy, 1991; Ishimaru, 1997) is used to obtain the total wavefield recorded at P as the sum of the interfering spherical waves reradiated by the point scatterers S according to the Huygens principle.

In a local cylindrical coordinates system (r, φ) with the $r = 0$ axis (i.e., the z axis) oriented vertically and passing through the receiver point P, the backscattered wavefield measured at point P is given by

$$\psi_\omega(P) = -\frac{i\psi_0}{\lambda} \int_0^{r_0} \int_0^{2\pi} \frac{(1+\cos\theta_e)}{2} \frac{e^{ik[d_e(r,\varphi)-h(r,\varphi)]}}{d_e(r,\varphi)} r \, dr \, d\varphi, \tag{10}$$

where $k = \omega/c$ is the wave number and d_e is the distance between P and each secondary source S (i.e., point scatterer) forming the rough surface. $h(r, \varphi)$ is the surface topography measured with respect to the altitude of the surface nadir point N located on the $r = 0$ axis, i.e., vertically and at a distance l_e below the receiver point P. The argument in the complex exponential represents the phase lag of the spherical wave arriving at the point P and coming from the point scatterer $S(r, \varphi, h)$ (Fig. 8). The h term actually represents the phase lag of the incident plane wave which excites the point scatterer, and which is transferred to the phase of the reradiated spherical wave. The term $(1 + \cos\theta_e)/2$ is the obliquity factor where θ_e is the backscattering angle. The maximum radius of integration r_0 must be chosen larger than the radius r_A of the Airy–Fresnel spot in order to be sure that the integral (10) correctly captures all constructive interferences producing the backscattered wavefield measured at P.

The far field hypothesis assumed in the model allows to make substantial simplifications in Eq. (10). The distance d_e

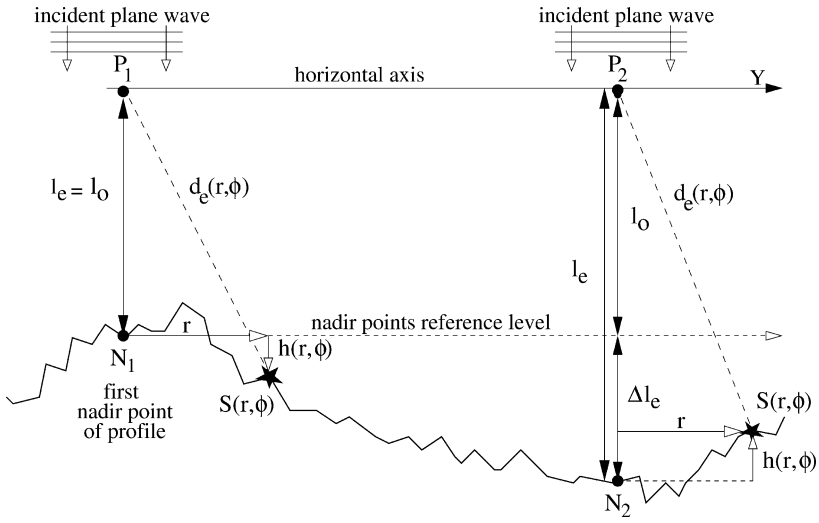

Fig. 8. Description of the experimental situation with the meanings of the symbols used in the models. The hydrophone is located at the points P_i and is translated along a horizontal y profile. Observe that the altitude l_e of the receiver points P_i above the corresponding nadir projections N_i varies from one measurement location to another (here P_1 and P_2). The backscattered waves are obtained by summing the waves reradiated by the point scatterers S forming the surface and shown as irregular star symbols.

between P and the point scatterer S on the surface may be written as

$$d_e(r,\varphi) = l_e\left[1 + \frac{r^2}{l_e^2} - 2\frac{r}{l_e}\sin\theta_e\cos(\varphi_e - \varphi) - 2\frac{h(r,\varphi)}{l_e}\cos\theta_e\right]^{1/2} \tag{11}$$

and, in the far field geometry, $l_e \gg r$, so $\theta_e \simeq 0$ and $r^2/l_e^2 \ll 1$. Under these conditions the formula giving the distance d_e may be simplified as

$$d_e(r,\varphi) \simeq l_e(r) - h(r,\varphi) \tag{12}$$

and the obliquity factor may be omitted in Eq. (10). Including these simplifications into (10), we obtain

$$\psi_\omega(P) = -\frac{i\psi_0}{\lambda}\frac{e^{ikl_e}}{l_e}\int_0^{r_0} r\,\mathrm{d}r\int_0^{2\pi} e^{-2ikh(r,\varphi)}\,\mathrm{d}\varphi. \tag{13}$$

The mean field $\langle\psi_\omega\rangle$ is obtained by integrating the backscattered field while translating the receiver point P above the surface along a horizontal y profile of length L. Let us emphasize that the altitude l_e of the receiver point P above its nadir projection N on the surface varies from one place to another along the profile (Fig. 8). Accounting for this fact, the mean field is given by

$$\langle\psi_\omega\rangle_{r_0,L} = -\frac{i\psi_0}{L\lambda}\int_0^{L}\frac{e^{ikl_e(y)}}{l_e(y)}\,\mathrm{d}y\int_0^{r_0} r\,\mathrm{d}r\int_0^{2\pi} e^{-2ikh(r,\varphi)}\,\mathrm{d}\varphi, \tag{14}$$

where the y-dependence of the distance l_e has been made explicit. The rightmost integral involving the azimuth φ may be stochastically evaluated by using the fact that the topography $h(r,\varphi)$ has a Gaussian distribution (Fig. 4) with a standard deviation $\xi_c(r)$ given by the power law obtained for circular sampling at scales L_c (Fig. 3). Replacing the φ integral by one over the h distribution at a given r we arrive at the Fourier transform of a Gaussian (see Shepard and Campbell, 1999, for details) and obtain:

$$\langle\psi_\omega\rangle_{r_0,L} = -\frac{i\psi_0}{L\lambda}\int_0^{L}\frac{e^{ikl_e(y)}}{l_e(y)}\,\mathrm{d}y\int_0^{r_0} e^{-2k^2\xi_c^2(r)}r\,\mathrm{d}r. \tag{15}$$

The stochastic integral along the averaging y profile may be computed by considering that the distance $l_e(y)$ may be written as

$$l_e(y) = l_0 + \Delta l_e(y), \tag{16}$$

where $l_0 = l_e(0)$ and $\Delta l_e(y)$ is the variation of altitude with respect to the initial altitude l_0 measured at the beginning of the profile. We assume that Δl_e obeys a Gaussian distribution with root mean square $\xi_Y(y)$ (Fig. 3). This assumption may be improved by using the correlation function of $\Delta l_e(y)$. Another correlation occurs if the sampling interval along the y profile is smaller than twice the radius r_A of the Airy–Fresnel spot. If the distance between the transducers and the surface is kept constant, i.e., $l_e(y) = l_0$, the random fluctuations $\Delta l_e(y)$ are no more considered and Eq. (15) reduces to the expression given by Shepard and Campbell (1999),

$$\langle\psi_\omega\rangle_{r_0} = -\frac{i\psi_0}{\lambda}\frac{e^{ikl_0}}{l_0}\int_0^{r_0} e^{-2k^2\xi_c^2(r)}r\,\mathrm{d}r. \tag{17}$$

Let us emphasize that this situation does not correspond to the experiments discussed in the present study and that the relevant equation is (15).

In Eq. (15) the mean backscattered field $\langle\psi_\omega\rangle$ is computed by evaluating the stochastic y integral through a Monte

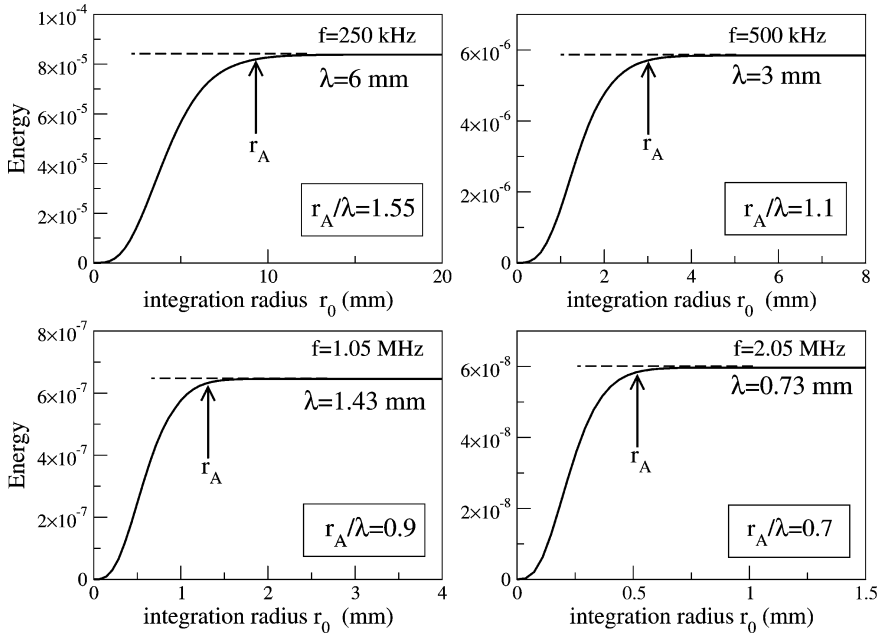

Fig. 9. Curves showing the evolution of the energy of the backscattered field as a function of the integration radius r_0. The radius r_A of the Airy–Fresnel spot is defined as the critical radius beyond which the energy level remains constant. The smaller the wavelength the smaller the r_A. Observe that the r_A/λ ratio decreases as the frequency increases, indicating that the roughness at the smaller scales more efficiently annihilates the backscattered field.

Carlo procedure and the r integral is computed with a deterministic integration method. For both models (15) and (17) the mean field is computed by using the statistical parameters estimated from the digitized topography of the sample rough surface and $l_0 = 600$ mm according to the experimental conditions. The frequency range is the same as the experimental one and goes from 172 to 2.572 MHz with a 10 kHz sampling interval. After computing the mean field $\langle\psi_\omega\rangle$, the energy is computed:

$$\left|\langle\psi_\omega\rangle\right|^2 = \left|\langle\psi_\omega\rangle\langle\psi_\omega\rangle^*\right|, \tag{18}$$

where $\langle\psi_\omega\rangle^*$ indicates the complex conjugate of the mean field.

Before comparing the model predictions with experimental data, we first check the validity of the far-field assumption $l_e \gg r_0$ used to obtain Eqs. (15) and (17). Figure 9 shows the energy of the mean backscattered field given by Eq. (17) as a function of the maximum integration radius r_0. It can be observed that the energy level ceases to increase beyond a limit radius r_A which can be identified as the Airy–Fresnel radius discussed above, and the maximum integration radius r_0 must be chosen greater than r_A in order to correctly integrate all the coherently-interfering waves reradiated by the point scatterers. As can be checked, the radius r_A is much smaller than the classical first Fresnel radius $r_F = \sqrt{\lambda l_e/2}$. This may be explained by the fact that the interfering waves reradiated by the point scatterers located on the circles with $r > r_A$ do not interfere coherently enough to contribute to the total wave packet received by the hydrophone. Indeed, the larger the radius r, the larger the topography variations occurring along the path L_c (Fig. 4), and the larger the destructive interferences. Interestingly, we observe that the radius r_A roughly corresponds to circles where the topography variations have a standard deviation close to $\lambda/4$. This can be verified for the circle with $r = 10$ mm shown on Fig. 4 and whose topography histogram has a standard deviation of 1.6 mm, i.e., about a quarter of the wavelength $\lambda = 6$ mm for which $r_A \simeq 9$ mm (Fig. 9). The frequency dependence of r_A is a consequence of the self-affine properties of the rough surface: the shorter the wavelength λ the shorter the path L_c (i.e., the radius r_c) necessary to have topography variations with a standard deviation equals to $\lambda/4$ (Fig. 9). These results point out that a self-affine surface leads to wavelength-dependent scattering (Shepard and Campbell, 1999). In all instances, the assumption $l_e \gg r$ is satisfied (recall that $l_e \simeq 600$ mm) and the coherence of the model is established.

5. Comparison with experimental results

We now turn to the comparison of the models given by Eqs. (15) and (17) with the experimental results. In all examples presented in the following, the amplitude term ψ_0 is experimentally determined in order to give the best fit between the model curves and the data. Figure 10 shows the data together with the theoretical curves corresponding to the model used by Shepard and Campbell (1999) (Eq. (17)). These curves only differ by their ψ_0 term, and it can be observed that the model curves agree with the spectra obtained by averaging a small number $n = 5$ and 10 of individual wavelet responses, i.e., along short y profiles ($L = 10$ and 22.5 mm). For $n = 75$ (i.e., $L = 185$ mm), the model curves cease to agree with the short-wavelength ($f > 500$ kHz)

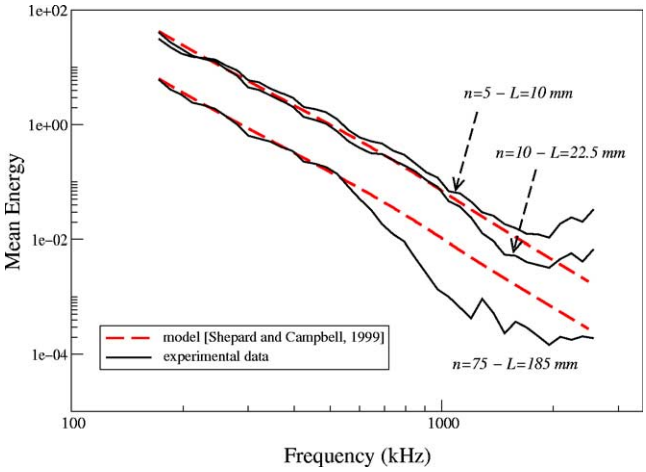

Fig. 10. Comparison between experimental data and synthetic data generated with the model proposed by Shepard and Campbell (1999). The experimental curves are shown for an increasing number n of averaged individual wavelet responses (see also Fig. 7). L is the length of the averaging y profile corresponding to the n averaged individual wavelet responses.

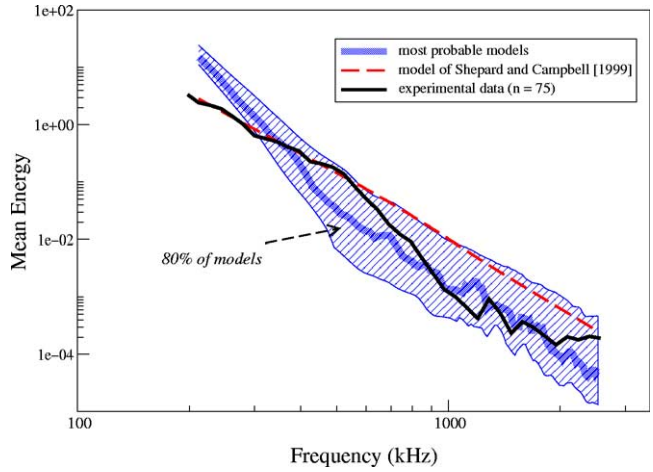

Fig. 11. Comparison between experimental data (for an averaging of $n = 75$ individual wavelet responses) and the stochastic model given by Eq. (15). The stochastic integration along the y profile of length $L = 185$ mm is done with Gaussian white topography profiles $l_e(y)$ (see text for details and the top part of Fig. 12 for an example of a profile). The shaded area represents 80% of 400 realizations of model curves, each one corresponding to a different stochastic integration along the y profile.

part of the data and predicts a larger energy than actually observed in this frequency domain. This may be explained by the fact that the model does not consider the random variations $\Delta l_e(y)$ of the distance $l_e(y)$ along the averaging profile. Indeed, and particularly in the short-wavelength domain, these variations produce large phase lags among the individual wavelet responses and destructive interference phenomena annihilate a larger part of the energy of the mean backscattered field. These effects are less efficient for larger wavelengths where the model continues to fit with the experimental curves.

The more complete stochastic model given by Eq. (15) accounts for the random variations $\Delta l_e(y)$ as one moves along the averaging profile. In a first step, the $\Delta l_e(y)$ are drawn from a white Gaussian distribution with root mean square $\xi_Y(y)$ (Fig. 3). Since the averaging profile has a finite length L the random drawing of the altitude variations $\Delta l_e(y)$ produces a different $l_e(y)$ profile at each time. As a result, the stochastic evaluation of the y integral through a Monte Carlo procedure gives a different value for each simulated y profile. As a consequence, the model has a stochastic nature instead of a deterministic one, and a comparison of the model against the experimental data must be done in a statistical sense. This is performed by synthesizing 400 topography profiles $l_e(y)$ of length L and by computing the corresponding 400 energy spectra with Eq. (15). The set of so-obtained spectra is used to construct a histogram of their distribution which is the relevant quantity to be compared with the data (see Tarantola and Valette, 1982, for details).

The dashed area in Fig. 11 represents the area covering 80% of the generated models, and the thick middle line represents the most probable models. It can be observed that most of the experimental curve falls in the 80% area, the misfit being restricted to the low frequencies ($f < 250$ kHz) where the energy predicted by the model exceeds the measured energy. This discrepancy may be due to the long-range correlation observed for the experimental rough surface (Fig. 1B) and which is not reproduced by the synthetic topography profiles which are white Gaussian noises (Fig. 12A). A further improvement of the model can be done by accounting for the long-range correlation of the topography variations $\Delta l_e(y)$ along the averaging profiles. Instead of constructing random altitude profiles $l_e(y)$ with a

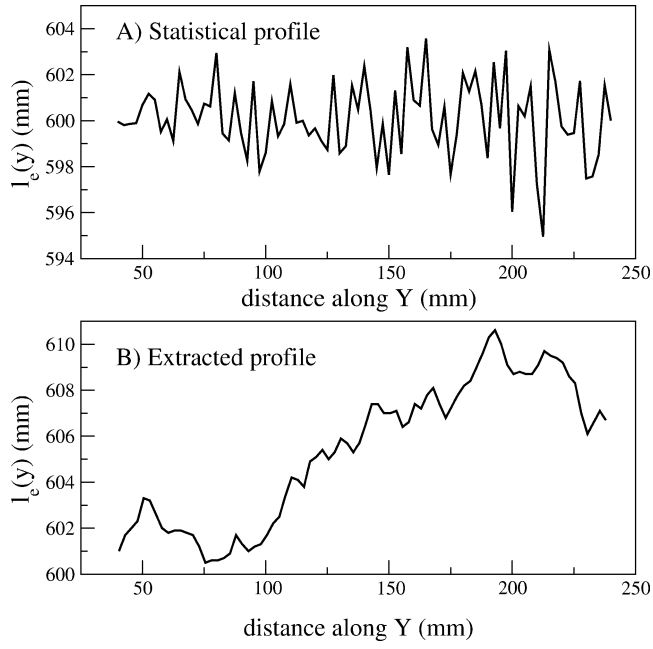

Fig. 12. Top part: example of a random topography profile $l_e(y)$ generated to construct the individual model curves whose statistics is shown on Fig. 11. The profile is a Gaussian white noise which does not properly account for the long-range correlation observed in the actual topography profiles, one of which is shown in the bottom part of the figure.

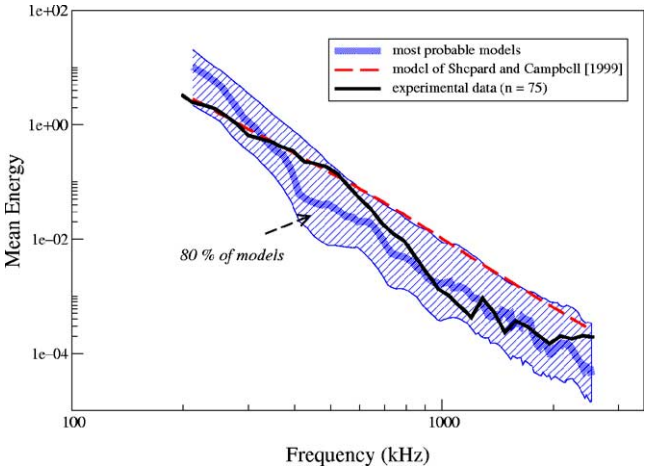

Fig. 13. Same as Fig. 11 but with a stochastic integration along the y profile of length $L = 185$ mm done by using 400 actual topography profiles $l_e(y)$ (as the one shown in the Bottom part of Fig. 12). The shaded area represents 80% of 400 realizations of model curves, each one corresponding to a different stochastic integration along the y profile.

long-range correlation, we prefer to use 400 y profiles extracted from the actual topography (Fig. 2), one of which is shown in Fig. 12B. At this point, it must be said that the extracted profiles come from the whole resin surface and not only from the neighborhood of the y profile scanned during the backscattering experiment. Using these more realistic profiles, 400 energy spectra are computed in the same manner as above and Fig. 13 shows the distribution of the corresponding model curves. It can be seen that accounting for the long-range correlation essentially modifies the low-frequency part of the curves by both widening the 80% area and slightly decreasing the average slope. The entire experimental curve now falls into the 80% area. In both cases (Figs. 11 and 13) the curve corresponding to the model of Shepard and Campbell (1999) has the correct energy slope in the low-frequency domain but is at the upper edge of the 80% areas in the high-frequency domain.

6. Conclusion

The acoustical setup presented in this paper allowed to perform a backscattering experiment over a self-affine rough surface for a wide-frequency range 172 kHz $\leqslant f \leqslant$ 2.572 MHz. This experiment is done in a near-nadir configuration and the energy spectrum of the backscattered field averaged along a profile is measured. A comparison with the model proposed by Shepard and Campbell (1999) (Eq. (17)) is performed and shows that the model agrees with the low-frequency part of the data (Fig. 10) but predicts a too-large energy at high frequencies. A refinement of the model is proposed by accounting for the self-affine variations of the surface topography along the averaging y profile (Eq. (15)). The resulting spectra are in better agreement with the high-frequency part of the experimental curves, showing the importance of the altitude variations along the averaging profile in the construction of the mean backscattered field. Because of the self-affine nature of the roughness, the averaging along a profile of moderate finite length L produces strong fluctuations of the mean field intensity from one realization (i.e., an averaging operation along a given y profile) to another. The same phenomena is observed for the modeled backscattered field so that a single model curve is unsuitable for comparison with the data. Instead, a statistical analysis of a population of model curves is used to account for the stochastic nature of the model.

Acknowledgments

We thank Michel Lemoine for is skilled assistance in designing the experimental setup. Frédéric Conil provided the simulated annealing algorithm to design the wavelet source signals. Michael Shepard and an anonymous Reviewer made very constructive comments which helped us to greatly improve the paper. This work is financially supported by the CNRS and ANDRA through the GdR FORPRO (Research action number 99.II) and corresponds to the GdR FORPRO contribution number 2003/04 A.

References

Bouchaud, E., Lapasset, G., Planès, J., 1990. Fractal dimension of fractured surfaces: a universal value. Europhys. Lett. 13, 73–79.

Bouchaud, E., 1997. Scaling properties of cracks. J. Phys. Condens. Matter 9, 4319–4344.

Brown, S.R., Scholz, C.H., 1985. Broad bandwidth study of the topography of natural rock surfaces. J. Geophys. Res. E 90, 12575–12582.

Brown, S.R., 1987. A note on the description of surface roughness using fractal dimension. Geophys. Res. Lett. 14, 1095–1098.

Campbell, B.A., Shepard, M.K., 1996. Lava flow surface roughness and depolarized radar scattering. J. Geophys. Res. E 101, 18941–18951.

Conil, F., Gibert, D., Nicollin, F., 2003. Nonlinear synthesis of input signals in ultrasonic experimental setups. J. Acoust. Soc. Am. In press.

Cox, B.L., Wang, J.S.Y., 1993. Fractal surfaces: measurement and applications in the Earth sciences. Fractals 1, 87–115.

Darboux, F., Huang, C.-H., 2003. An instantaneous-profile laser scanner to measure soil surface microtopography. Soil Sci. Soc. Am. J. 67, 92–99.

Elmore, W.C., Heald, M.A., 1985. Physics of Waves. Dover, New York.

Feder, J., 1988. Fractals. Plenum, New York.

Goodman, J.W., 1968. Introduction to Fourier Optics. McGraw–Hill, San Francisco.

Hastings, H.M., Sugihara, G., 1993. Fractals: A User's Guide for Natural Sciences. Oxford Univ. Press, Oxford.

Ishimaru, A., 1997. Propagation and Scattering in Random Media. IEEE Press/Oxford Univ. Press. Classic reissue.

Korvin, G., 1992. Fractal Models in the Earth Sciences. Elsevier, Amsterdam.

Le Gonidec, Y., Gibert, D., Proust, J.-N., 2002. Multiscale analysis of waves reflected by complex interfaces: basic principles and experiments. J. Geophys. Res. 107 (B9), 2184. doi: 10.1029/2001JB000558.

Mandelbrot, B., 1982. The Fractal Geometry of Nature. Freeman, San Francisco.

Mehrabi, A.R., Rassamdana, H., Sahimi, M., 1997. Characterization of long-range correlations in complex distributions and profiles. Phys. Rev. E 56, 712–722.

Ogilvy, J.A., 1991. Theory of wave scattering from random rough surface. Institute of Physics Publishing (IOP Ltd.), Philadelphia.

Poon, C.Y., Sayles, R.S., Jones, T.A., 1992. Surface measurement and fractal characterization of naturally fractured rocks. J. Phys. D Appl. Phys. 25, 1269–1275.

Power, W.L., Tullis, T.E., 1987. Roughness of natural fault surfaces. Geophys. Res. Lett. 14, 29–32.

Power, W.L., Tullis, T.E., 1991. Euclidean and fractal models for the description of the rock surface roughness. J. Geophys. Res. 97, 15425–15435.

Power, W.L., Tullis, T.E., 1992. The contact between opposing fault surfaces at Dixie Valley, Nevada, and implications for fault mechanics. J. Geophys. Res. 97, 15425–15435.

Schmittbuhl, J. , Schmitt, F., Scholz, C.H., 1995. Scaling invariance of crack surfaces. J. Geophys. Res. 100, 5953–5973.

Sayles, R.S., Thomas, T.R., 1978. Surface topography as a nonstationary random process. Nature 271, 431–434.

Shepard, M.K., Brackett, R.A., Arvidson, R.E., 1995. Self-affine (fractal) topography: surface parameterization and radar scattering. J. Geophys. Res. E 100, 11709–11718.

Shepard, M.K., Campbell, B.A., 1999. Radar scattering from a self-affine fractal surface: near-nadir regime. Icarus 141, 156–171.

Shepard, M.K., Campbell, B.A., Bulmer, M.H., Farr, T.G., Gaddis, L.R., Plaut, J.J., 2001. The roughness of natural terrain: a planetary and remote sensing perspective. J. Geophys. Res. E 106, 32777–32795.

Simonsen, I., Vandembroucq, D., Roux, S., 2000. Wave scattering from self-affine surfaces. Phys. Rev. E 61, 5914–5917.

Tarantola, A., Valette, B., 1982. Inverse problems = quest for information. J. Geophys. 50, 159–170.

Turcotte, D.L., 1997. Fractals and Chaos in Geology and Geophysics, 2nd edition. Cambridge Univ. Press, New York.

Voronovich, A.G., 1994. Wave Scattering from Rough Surfaces. Spinger-Verlag, Berlin.